Mechanical modeling of helical structures accounting for translational invariance. Part 2 : Guided wave propagation under axial loads

Fabien Treyssède, Ahmed Frikha, Patrice Cartraud

Mechanical modeling of helical structures accounting for translational invariance. Part 2 : Guided wave propagation under axial loads

Fabien Treyssède[a,*], Ahmed Frikha[a], Patrice Cartraud[b]

[a] *LUNAM Université, IFSTTAR, MACS, F-44344 Bouguenais, France*
[b] *LUNAM Université, GeM, UMR CNRS 6183, Ecole Centrale de Nantes, 1 rue de la Noë, 44 321 Nantes Cédex 3, France*

Abstract

This paper corresponds to the second part of a study that aims at modeling helical structures accounting for translational invariance. In the Part 1 of this paper, the static behavior has been addressed using a helical homogenization approach which provides the stress state corresponding to axial loads. The latter is considered as a prestressed state, for elastic wave propagation analysis in helical waveguides, which is the subject of the Part 2 of this paper. Non destructive testing of springs and multi-wire strands is a potential application of the proposed model. Accounting for translational invariance, the elastodynamic equations of prestressed helical structures yield a 2D problem posed on the cross-section, corresponding to a so-called semi-analytical finite element (SAFE) formulation. For helical springs, the numerical model is validated with an analytical solution corresponding to a Timoshenko beam approximation. It is shown that the influence of the prestressed state is significant at low frequencies. Finally, a seven-wire strand subjected to axial loads is considered. The computed dispersion curves are compared to experimental data. Good agreement is obtained for the first compressional-like modes and their veering central frequency.

Keywords: Waveguide; Prestress; Helical coordinates; Finite element;

*Corresponding author
Email address: fabien.treyssede@ifsttar.fr (Fabien Treyssède)

Strands; Springs.

---

1. Introduction

This paper is the second part of a study that aims at modeling helical structures accounting for translational invariance. In Part 1, the static state in the case of axial loads has been addressed. Taking into account the effects of prestress and geometry deformation due to these static loads, the objective of Part 2 is the computation of wave modes guided by the helical structures.

Inspection methods based on elastic guided waves are among the most popular techniques of non destructive testing. Due to the complexity of signals, this technique is often restricted to simple geometries such as plates and pipes. The computation of modes of propagation in more complex geometries (arbitrary cross-section, curved axis,...) requires appropriate simulation tools, typically based on finite element methods.

A first method based on the Floquet conditions, applicable to periodic structures, has been used for straight structures (Gry and Gontier (1997); Duhamel et al. (2006); Mencik and Ichchou (2007)) and for helical waveguides (Treyssède (2007)). A more efficient method, valid for translationally invariant structures and often referred to as the semi-analytical finite element (SAFE) method, has also been developed. This technique has been proposed in early works in Dong and Nelson (1972). With this method, the problem is reduced on the cross-section, which decreases the computation time. More recently, the SAFE method has been used for straight waveguides with arbitrary cross-section (Gavric (1995); Damljanovic and Weaver (2004); Hayashi et al. (2006); Jezzine (2006)) or material complexity (Rattanawangcharoen et al. (1992); Zhuang et al. (1999); Bartoli et al. (2006); Marzani (2008)). This approach has also been applied to curved waveguides: twisted in Onipede and Dong (1996), toroidal in Demma et al. (2005) and Finnveden and Fraggstedt (2008) and helical in Treyssède (2008). Finally, a SAFE method modeling the propagation of elastic waves in seven-wire strands has been developed in Treyssède and Laguerre

(2010).

Helical structures such as springs and strands are generally subjected to axial loads. The above-mentioned works are restricted to the propagation of guided waves in unloaded structures. Only few studies have extended the SAFE method to loaded waveguides. Straight waveguides under axial loads have been considered in Chen and Wilcox (2007) and Loveday (2009). To the authors knowledge, there is no general model in the literature that allows to determine guided modes propagating in prestressed curved waveguides.

Therefore the goal of this paper is to propose a numerical model for the propagation of guided waves in helical structures subjected to axial loads, particularly in prestressed multi-wire strands. This study is limited to linear elastic materials. The SAFE method is adopted, which allows to solve the 3D elastodynamic equations of motion thanks to a 2D model and without beam approximation.

The method developed in this paper is restricted to multi-wire helical structures composed of a stack of helical wires wrapped with the same twisting rate around a straight axis. As explained in Section 3 of Part 1, this excludes the case of double helical structures (such as independent wire rope core for instance) and cross-lay strands.

The paper is organized as follows. Considering the static state computed in Part 1 as the prestressed state, the variational formulation associated with the superimposed linear dynamics is first described in Section 2. The twisting coordinate system is then introduced and differential operators are expressed in this system in Section 3. Exploiting the translational invariance property, the 3D variational formulation is then reduced in Section 4 to a 2D problem posed on the cross-section, which is classical in the framework of SAFE methods. In Section 5, an energy velocity expression is derived for prestressed waveguides. Using SAFE matrices, the equality between group and energy velocities is proved for undamped materials. Then for helical springs, numerical results are compared in Section 6 to those of a beam model proposed in Frikha et al. (2011). For seven-wire strands subjected to axial loads, using stick contact conditions between the

core and peripheral wires, numerical results are compared to experimental data in Section 7.

2. Dynamic motion of prestressed structures

The analysis of the dynamics of prestressed structures can be decomposed into a static problem, solved in Part 1 of this paper, and the motion superimposed on this prestressed state, which is the aim of Part 2. Therefore, three configurations must be distinguished: the initial configuration (without initial stress), the prestressed static configuration (which is denoted V_0) and the final configuration including dynamics. An updated Lagrangian formulation is used, the variables being expressed in the prestressed static configuration.

One assumes a linear and elastic material behavior and a time-harmonic $e^{-i\omega t}$ evolution of the solution. Considering small-amplitude waves as perturbations onto the prestressed static state, the 3D variational formulation governing elastodynamics is given by (see e.g. Bathe (1996) and Yang and Kuo (1994)):

$$\begin{aligned} \forall \delta\mathbf{u}, \int_{V_0} \delta\boldsymbol{\epsilon} \colon \mathbf{C}_0 \colon \boldsymbol{\epsilon}\, dV_0 + \int_{V_0} \mathrm{tr}(\nabla_0 \delta\mathbf{u} \cdot \boldsymbol{\sigma}_0 \cdot \nabla_0 \mathbf{u}^T) dV_0 \\ -\omega^2 \int_{V_0} \rho_0 \delta\mathbf{u} \cdot \mathbf{u} dV_0 = 0, \end{aligned} \tag{1}$$

with $\delta\mathbf{u}$ kinematically admissible and where $\mathbf{u}$ and $\boldsymbol{\epsilon} = 1/2(\nabla_0\mathbf{u} + \nabla_0\mathbf{u}^T)$ denote the displacement and the strain tensor, respectively. The subscript 0 refer to the prestressed static configuration: $\mathbf{C}_0$, ρ_0 and V_0 denote the elasticity tensor, the material density and the structural volume in the prestressed configuration. $\mathrm{tr}(\cdot)$ is the trace and ∇_0 is the gradient operator with respect to the prestressed configuration. $\boldsymbol{\sigma}_0$ is the Cauchy prestress, i.e. the stress tensor associated with the prestressed state. The second term of the formulation, related to $\boldsymbol{\sigma}_0$, is sometimes referred to as the geometric stiffness in the literature.

In the context of non-linear mechanics, Eq. (1) is the so-called linearized updated Lagrangian formulation, representing the motion of small perturbations superimposed on a given state. Its derivation requires a non-linear geometrical

analysis (large displacement or strain). This implies that the prestressed configuration should correspond to a non-linear geometrical state. Yet in this paper, one will assume that the effects of non-linearity of the prestressed state can be neglected on dynamics, and the linear computations of Part 1 will be used for simplicity.

3. Formulation in the curvilinear coordinate system

For the wave propagation analysis in curved waveguides, the variational formulation described in Section 2 must be expressed in an appropriate curvilinear coordinate system. In this paper, a coordinate system that satisfies translational invariance both for helical single-wire and multi-wire waveguides is required. Therefore, the twisted basis is chosen. The translational invariance property will be checked in Section 4. The reader may refer to Part 1 of this paper for more details.

3.1. Twisted basis

One considers a helical single-wire waveguide (see Fig. 1 in Part 1). Let $(\mathbf{e}_X, \mathbf{e}_Y, \mathbf{e}_Z)$ denotes the Cartesian orthonormal basis. The centreline is defined by a helix of radius R in the Cartesian plane $(\mathbf{e}_X, \mathbf{e}_Y)$ and pitch L along the Z-axis. The helix lay angle Φ is defined by $\tan\Phi = 2\pi R/L$.

The twisted basis $(\mathbf{e}_x, \mathbf{e}_y, \mathbf{e}_Z)$ has been defined in Part 1, as an orthonormal basis rotating around the Z-axis. It corresponds to a particular case of helical system with $\kappa = 0$ and $\tau = 2\pi/L$, where κ and τ denote the curvature and the torsion respectively. The unit vectors $\mathbf{e}_x$ and $\mathbf{e}_y$ are expressed in the Cartesian basis by Eq. (3) of Part 1.

However throughout Part 2, geometrical parameters R, L, Φ, κ and τ are now associated with the prestressed configuration, i.e. the deformed helix under the action of the static axial load. Rigorously, these parameters should be denoted with subscripts 0, omitted for brevity's sake of notations throughout Part 2. When needed, we will use subscripts i (R_i or Φ_i for instance) to refer

to the initial geometrical parameters, i.e. parameters associated with the initial configuration (without initial stress).

In order to express differential operators in the twisted basis, one has to develop them in the covariant and contravariant bases, ($\mathbf{g}_1$,$\mathbf{g}_2$,$\mathbf{g}_3$) and ($\mathbf{g}^1$,$\mathbf{g}^2$,$\mathbf{g}^3$), which have been defined by Eqs. (5) and (7) in Part 1.

One recalls that the Christoffel symbol of the second kind Γ_{ij}^k can be calculated from $\Gamma_{ij}^k = \mathbf{g}_{i,j} \cdot \mathbf{g}^k$, where $\mathbf{g}_{i,j}$ corresponds to the derivatives of the covariant basis. Its expression in the twisted basis has been obtained in Eq. (8) of Part 1.

As a side remark, note that twisting coordinates have also been used for elastic wave propagation in pretwisted beams (Onipede and Dong (1996)), for electromagnetic waves in optical helical waveguides (Nicolet et al. (2004); Nicolet and Zola (2007)) and for twisted electrostatic problems (Nicolet et al. (2007)).

3.2. Differential operators

The differential operators involved in the variational formulation (1) are the gradient and the strain operators. As explained in Part 1 of this study, they have first to be expressed in the covariant and contravariant bases (see e.g. Chapelle and Bathe (2003), Synge and Schild (1978), Wempner (1981)).

The gradient tensor ∇_0 is defined in the contravariant basis as:

$$\nabla_0 \mathbf{u} = \gamma_{ij} \mathbf{g}^i \otimes \mathbf{g}^j \ , \ \gamma_{ij} = u_{i,j} - \Gamma_{ij}^k u_k, \tag{2}$$

where u_i denotes the covariant displacement.

Using the relation between the contravariant and the twisted vectors (Eq. (7) of Part 1), the gradient tensor can be expressed in the twisted basis under the following vector form:

$$\{\gamma\} = (\mathbf{G}_{xy} + \mathbf{G}_Z \frac{\partial}{\partial Z})\{u\}, \tag{3}$$

with:

$$\mathbf{G}_{xy} = \begin{bmatrix} \partial/\partial x & 0 & 0 \\ \partial/\partial y & 0 & 0 \\ \Lambda & -\tau & 0 \\ 0 & \partial/\partial x & 0 \\ 0 & \partial/\partial y & 0 \\ \tau & \Lambda & 0 \\ 0 & 0 & \partial/\partial x \\ 0 & 0 & \partial/\partial y \\ 0 & 0 & \Lambda \end{bmatrix}, \mathbf{G}_Z = \begin{bmatrix} 0 & 0 & 0 \\ 0 & 0 & 0 \\ 1 & 0 & 0 \\ 0 & 0 & 0 \\ 0 & 0 & 0 \\ 0 & 1 & 0 \\ 0 & 0 & 0 \\ 0 & 0 & 0 \\ 0 & 0 & 1 \end{bmatrix}, \tag{4}$$

where $\Lambda = \tau(y\partial/\partial x - x\partial/\partial y)$. The column vectors $\{u\} = [u_x\, u_y\, u_Z]^T$ and $\{\gamma\} = [\gamma_{xx}\, \gamma_{xy}\, \gamma_{xZ}\, \gamma_{yx}\, \gamma_{yy}\, \gamma_{yZ}\, \gamma_{Zx}\, \gamma_{Zy}\, \gamma_{ZZ}]^T$ are the displacement and gradient components respectively.

Following Part 1, the strain vector is related to the displacement vector in the twisted basis through: $\{\epsilon\} = (\mathbf{L}_{xy} + \mathbf{L}_Z \frac{\partial}{\partial Z})\{u\}$, where $\{\epsilon\} = [\epsilon_{xx}\, \epsilon_{yy}\, \epsilon_{ZZ}\, 2\epsilon_{xy}\, 2\epsilon_{xZ}\, 2\epsilon_{yZ}]^T$ is the strain vector. $\mathbf{L}_{xy}$ and $\mathbf{L}_Z$ have the expression given by Eq. (10) of Part 1, recalling that this time the geometrical parameter τ corresponds the torsion of the geometry in the prestressed state.

3.3. Material properties

Mechanical properties are strain-dependent but under the small strain assumption, which is used in this paper, the elasticity tensor is the same in the reference and prestressed configurations, hence $\mathbf{C}_0 = \mathbf{C}$ (Bathe (1996); Yang and Kuo (1994)). Its expression in the twisted basis, which is orthonormal, has been given in Eq. (12) of Part 1.

Besides the change of material density between the reference and prestressed states can also be neglected ($\rho_0 = \rho$).

3.4. Variational formulation

The variational formulation given by Eq. (1), is now rewritten in a suitable matrix form based on the displacement, strain and gradient vectors previously

defined. It can be shown that one has:

$$\mathrm{tr}(\nabla_0 \delta\mathbf{u} \cdot \boldsymbol{\sigma}_0 \cdot \nabla_0 \mathbf{u}^T) = \{\delta\gamma\}^T [\Sigma_0] \{\gamma\}, \tag{5}$$

where the matrix $[\Sigma_0]$ is defined as follows:

$$[\Sigma_0] = \begin{bmatrix} [\sigma_0] & 0 & 0 \\ 0 & [\sigma_0] & 0 \\ 0 & 0 & [\sigma_0] \end{bmatrix}, [\sigma_0] = \begin{bmatrix} \sigma_{0_{xx}} & \sigma_{0_{xy}} & \sigma_{0_{xZ}} \\ \sigma_{0_{yx}} & \sigma_{0_{yy}} & \sigma_{0_{yZ}} \\ \sigma_{0_{Zx}} & \sigma_{0_{Zy}} & \sigma_{0_{ZZ}} \end{bmatrix}. \tag{6}$$

Note that the components of $[\sigma_0]$ must be expressed in the twisted basis associated with the prestressed configuration.

Finally, the variational formulation of the elastodynamics of prestressed structures (1) becomes:

$$\begin{aligned} \forall \delta u, \int_{V_0} \{\delta\epsilon\}^T [C_0] \{\epsilon\} dxdydZ + \int_{V_0} \{\delta\gamma\}^T [\Sigma_0] \{\gamma\} dxdydZ \\ -\omega^2 \int_{V_0} \rho_0 \{\delta u\}^T \{u\} dxdydZ = 0. \end{aligned} \tag{7}$$

4. SAFE method

In this section, a SAFE method is applied starting from the formulation (7). This method consists in assuming wave fields with a harmonic axial dependence. The displacement field is thus of the form:

$$\mathbf{u} = \mathbf{u}(x, y) e^{i(kZ - \omega t)}. \tag{8}$$

The first term represents the displacement field in the cross-section. The second corresponds to an exponential e^{ikZ} representing wave traveling along the axis, k being the axial wavenumber, and to the time-harmonic dependence as already mentioned in Section 2. SAFE methods only require finite element (FE) discretization of the cross-section, which is advantageous since it reduces the problem from three to two dimensions.

The SAFE method has been thoroughly presented for straight waveguides in the literature (see for instance Gavric (1995); Hayashi et al. (2006); Bartoli et al. (2006)). For details on the extension of the SAFE method to helical waveguides, the reader may refer to Treyssède (2008) or Treyssède and Laguerre (2010).

4.1. Translational invariance

Assuming an e^{ikZ} dependence implies that axial and transverse variables must be separable in the governing equations of motion. This requires that the problem must be translationally invariant along the Z-axis in the twisted coordinate system.

As proved in Treyssède (2011), three conditions are sufficient for translational invariance of curved waveguides. These conditions, checked in Part 1 for the statics of springs and seven-wire strands, are recalled here for clarity:

1. The material properties do not vary along the Z-axis in the twisted coordinate system;

2. The coefficients of the differential operators are independent on the axial variable Z;

3. The cross-section does not varies along the Z-axis in the twisted coordinate system.

Conditions 1 and 3 have already been proved in Part 1. Condition 2 must be checked for the dynamics of prestressed waveguides. A closer look at Eq. (1) shows that $\nabla_0 \mathbf{u}$ and the Cauchy prestress tensor $\boldsymbol{\sigma}_0$ must be independent on Z.

With regard to the gradient operator, its coefficients do not depend on Z in the twisted coordinate system (this is due to the independence on Z of the Christoffel symbol, as already noticed in Part 1). As for $\boldsymbol{\sigma}_0$, we have to require that the prestressed state does not vary along the Z-axis. In practice, under axial loads applied at the end cross-sections of the helical structure, this condition is fulfilled far from the ends. Therefore, the static prestressed state is invariant along the axis.

As already examined in Section 3 of Part I, translational invariance in multilayer wire ropes is also satisfied if the torsion of each wire remains identical (the numerical method proposed in this paper is still applicable). However, translational invariance is not fulfilled in cross-lay strands as well as double helical structures such as independent wire rope core.

4.2. SAFE formulation

Following the SAFE approach, the displacement vector and its test field are rewritten under the form (8) (Treyssède (2008); Treyssède and Laguerre (2010)). The displacement fields dependence in e^{ikZ} allows to replace the axial derivatives $\partial/\partial Z$ by ik. The variational formulation (7) then reduces to a 2D problem posed on the cross-section S_0. The SAFE variational formulation is:

$$\begin{aligned}
&\forall\{\delta u\}, \int_{S_0} \{\delta u\}^T (\mathbf{L}_{xy}^T[C_0]\mathbf{L}_{xy} + \mathbf{G}_{xy}^T[\Sigma_0]\mathbf{G}_{xy})\{u\}dxdy \\
&+ik \int_{S_0} \{\delta u\}^T (\mathbf{L}_{xy}^T[C_0]\mathbf{L}_Z - \mathbf{L}_Z^T[C_0]\mathbf{L}_{xy} + \mathbf{G}_{xy}^T[\Sigma_0]\mathbf{G}_Z \\
&\qquad -\mathbf{G}_Z^T[\Sigma_0]\mathbf{G}_{xy})\{u\}dxdy \\
&+k^2 \int_{S_0} \{\delta u\}^T (\mathbf{L}_Z^T[C_0]\mathbf{L}_Z + \mathbf{G}_Z^T[\Sigma_0]\mathbf{G}_Z)\{u\}dxdy \\
&\qquad -\omega^2 \int_{S_0} \rho_0 \{\delta u\}^T \{u\}dxdy = 0.
\end{aligned} \tag{9}$$

The finite element approximation is defined by $\{u\} = [N^e]\{U^e\}$, where $[N^e]$ is the matrix of the shape functions and $\{U^e\}$ the vector of nodal displacements, with 3 degrees of freedom per node. The FE discretization of Eq. (9) leads to the following eigenvalue problem:

$$\{[K_{1\sigma}] - \omega^2[M] + ik([K_{2\sigma}] - [K_{2\sigma}]^T) + k^2[K_{3\sigma}]\}\{U\} = 0, \tag{10}$$

where the element matrices are expressed as:

$$
\begin{aligned}
[M^e] &= \int_{S_0^e} \rho_0 [N^e]^T [N^e] dxdy, \\
[K_{1\sigma}^e] &= [K_1^e] + \int_{S_0^e} [N^e]^T \mathbf{G}_{xy}^T [\Sigma_0] \mathbf{G}_{xy} [N^e] dxdy, \\
[K_{2\sigma}^e] &= [K_2^e] + \int_{S_0^e} [N^e]^T \mathbf{G}_{xy}^T [\Sigma_0] \mathbf{G}_Z [N^e] dxdy, \\
[K_{3\sigma}^e] &= [K_3^e] + \int_{S_0^e} [N^e]^T \mathbf{G}_Z^T [\Sigma_0] \mathbf{G}_Z [N^e] dxdy, \\
[K_1^e] &= \int_{S_0^e} [N^e]^T \mathbf{L}_{xy}^T [C_0] \mathbf{L}_{xy} [N^e] dxdy, \\
[K_2^e] &= \int_{S_0^e} [N^e]^T \mathbf{L}_{xy}^T [C_0] \mathbf{L}_Z [N^e] dxdy, \\
[K_3^e] &= \int_{S_0^e} [N^e]^T \mathbf{L}_Z^T [C_0] \mathbf{L}_Z [N^e] dxdy.
\end{aligned}
\tag{11}
$$

The second term of the right hand side in the expressions of $[K_{1\sigma}^e]$, $[K_{2\sigma}^e]$ and $[K_{3\sigma}^e]$ correspond to the so-called geometric stiffness effect (second term of formulation (1)), related to the presence of a prestress field ($\boldsymbol{\sigma}_0 \neq \mathbf{0}$). Note that the SAFE formulation given by Eqs. (10)-(11) for prestressed helical structures degenerates to the unprestressed case (Treyssède and Laguerre (2010)) if $[\Sigma_0] = 0$ and $S_0 = S$.

The matrice $[K_1^e]$ is the same as the matrix $[K^e]$ defined in Part 1 for the static problem, except that the integration is now performed on the prestressed configuration S_0 (instead of S), accounting for the geometry deformation.

In practice, the cross-section mesh of the prestressed structure is obtained as follows. The cross-section of the structure without initial stress is first meshed. The prestressed state is computed based on this mesh. Then, the position of nodes is updated to provide the mesh of the cross-section S_0 in the prestressed configuration. The guided modes are computed on this updated mesh.

The solution of the eigensystem (10) yields the modes of propagation. It can be noticed that $[K_{1\sigma}]$, $[K_{3\sigma}]$ and $[M]$ are symmetric. Hence for an eigenvalue k, $-k$ is also an eigenvalue. This problem has then two kinds of eigensolutions: (k_i, U_i^+) and $(-k_i, U_i^-)$ for $i = 1, ..., n$ (n being the number of degrees

of freedom), representing n modes traveling in the positive direction and n modes in the negative direction. For undamped materials, pure real and imaginary wavenumbers represent propagating and evanescent modes, respectively. Complex wavenumber are referred to as inhomogeneous modes (such modes are oscillatory but decay after a few oscillations). Pure real and imaginary solutions appear in pairs of opposite signs and complex solutions appear in quadruple of opposite signs and complex conjugates.

The eigensystem (10) can be solved by setting the wavenumber k and finding the frequency ω or inversely. For propagating modes in undamped materials, the eigenvalue system can be solved by setting a real positive wavenumber k. The system is then linear in ω^2. For non-propagating modes or for damped materials, wavenumbers become complex and the problem must be solved by setting ω and finding k. The eigensystem is then quadratic in k and the system should be linearized (Tisseur and Meerbergen (2001)).

In this study our concern is propagating modes. Thereafter, eigensolutions are obtained by finding frequencies associated with real wavenumbers.

5. Modal velocities

The goal of this section is to formally derive group and energy modal velocities expressions in prestressed waveguides.

5.1. Group velocity

For a real wavenumber k, the phase and group velocities are defined by $V_\phi = \omega/k$ and $V_g = \partial\omega/\partial k$, respectively. For undamped materials and propagating modes, the SAFE expression of group velocity has been obtained for unprestressed structures in Bartoli et al. (2006) and Finnveden (2004). The method consists in differentiating with respect to k the SAFE eigenproblem. In the presence of prestress, the eigenproblem (10) to be solved remains quadratic and keeps the same general form as its unprestressed counterpart. As a consequence, the expression derived in the above-mentioned references can be directly

extended to the prestress case, which yields:

$$V_g = \frac{1}{2\omega} \frac{\{U\}^{T*}(i([K_{2\sigma}] - [K_{2\sigma}]^T) + 2k[K_{3\sigma}])\{U\}}{\{U\}^{T*}[M]\{U\}}, \tag{12}$$

where as shown in Section 4.2, matrices $[K^e_{2\sigma}]$ and $[K^e_{3\sigma}]$ account for geometric stiffness effects. The above expression has also been used in Loveday (2009) for straight waveguides subjected to axial loads.

5.2. Energy velocity

The energy velocity is defined as the ratio between the transmitted power and the stored energy, averaged in time and in the cross-section (see e.g. Achenbach (1973)):

$$V_e = \frac{\int_{S_0} \overline{\mathbf{P}} \cdot \mathbf{n} dS_0}{\int_{S_0} (\overline{E}_k + \overline{E}_p) dS_0}, \tag{13}$$

where the bar denotes time average and $\mathbf{n}$ is the unit vector normal to the cross-section. $\mathbf{P}$, E_k and E_p are the Poynting vector, the kinetic energy density and the potential energy density, respectively.

To the authors knowledge, the above definition has mainly been applied to structures without initial stress. Hence, one needs to properly define $\mathbf{P}$, E_k and E_p in the presence of prestress.

For prestressed structures, the strong form corresponding to the variational formulation (1) is:

$$\nabla_0 \cdot (\mathbf{C}_0 \colon \boldsymbol{\epsilon} + \nabla_0 \mathbf{u} \cdot \boldsymbol{\sigma}_0) = \rho_0 \ddot{\mathbf{u}}. \tag{14}$$

It can be checked that this equilibrium equation indeed derives from a Lagrangian density L, where $L = E_k - E_p$ with:

$$E_k = \frac{1}{2} \rho_0 \dot{\mathbf{u}} \cdot \dot{\mathbf{u}}, \tag{15}$$

and:

$$E_p = \frac{1}{2} \boldsymbol{\epsilon} \colon \mathbf{C}_0 \colon \boldsymbol{\epsilon} + \frac{1}{2} \mathrm{tr}(\nabla_0 \mathbf{u} \cdot \boldsymbol{\sigma}_0 \cdot \nabla_0 \mathbf{u}^T). \tag{16}$$

Concerning the Poynting vector (i.e. the power flow per unit area), it can be calculated thanks to the Lagrangian density from: $P_J = \dot{u}_I \partial L / \partial u_{I,J}$ (here,

index notation is used in the Cartesian coordinate system with the Einstein summation convention). Calculations yield:

$$\mathbf{P} = -\dot{\mathbf{u}} \cdot (\mathbf{C}_0 \colon \boldsymbol{\epsilon} + \nabla_0 \mathbf{u} \cdot \boldsymbol{\sigma}_0). \tag{17}$$

When $\boldsymbol{\sigma}_0 = \mathbf{0}$, Eqs. (16) and (17) degenerate to the well known energy and power flow expressions without prestress (see Achenbach (1973) for instance).

From SAFE matrices, it can be easily checked that:

$$\begin{aligned} &\int_{S_0} \overline{E}_k dS_0 = \frac{\omega^2}{4} Re(\{U\}^{T*}[M]\{U\}), \int_{S_0} \overline{E}_p dS_0 = \\ &\frac{1}{4} Re\left(\{U\}^{T*}([K_{1\sigma}] + ik([K_{2\sigma}] - [K_{2\sigma}]^T) + k^2[K_{3\sigma}])\{U\}\right). \end{aligned} \tag{18}$$

The computation of the cross-section and time averaged Poynting vector requires further developments (Treyssède (2008); Benmeddour et al. (2011)). Replacing the normal vector $\mathbf{n}$ by $\mathbf{e}_Z$ and averaging the Poynting vector, we obtain:

$$\int_{S_0} \overline{\mathbf{P}} \cdot \mathbf{n} dS_0 = \frac{\omega}{2} Im\left(\int_{S_0} u_\alpha^* (\mathbf{C}_0 \colon \boldsymbol{\epsilon} + \nabla_0 \mathbf{u} \cdot \boldsymbol{\sigma}_0)_{\alpha Z} dS_0\right), \tag{19}$$

where $\alpha = x, y, Z$. The integrand can be written as $u_\alpha^* (\mathbf{C}_0 \colon \boldsymbol{\epsilon} + \nabla_0 \mathbf{u} \cdot \boldsymbol{\sigma}_0)_{\alpha Z} = \{u\}^{T*}(\mathbf{L}_Z^T[C_0](\mathbf{L}_{xy} + ik\mathbf{L}_Z) + \mathbf{G}_Z^T[\Sigma_0](\mathbf{G}_{xy} + ik\mathbf{G}_Z))\{u\}$. Eq. (19) becomes:

$$\int_{S_0} \overline{\mathbf{P}} \cdot \mathbf{n} dS_0 = \frac{\omega}{2} Im\left(\{U\}^{T*}([K_{2\sigma}]^T + ik[K_{3\sigma}])\{U\}\right). \tag{20}$$

Finally, Eqs. (18) and (20) yield a direct computation of energy velocity from SAFE matrices:

$$V_e = \frac{2\omega Im\left(\{U\}^{T*}([K_{2\sigma}]^T + ik[K_{3\sigma}])\{U\}\right)}{Re\left(\{U\}^{T*}(\omega^2[M] + [K_{1\sigma}] + ik([K_{2\sigma}] - [K_{2\sigma}]^T) + k^2[K_{3\sigma}])\{U\}\right)}. \tag{21}$$

This equation degenerates to the unprestressed case, for which $[K_{1\sigma}] = [K_1]$, $[K_{2\sigma}] = [K_2]$ and $[K_{3\sigma}] = [K_3]$ becomes the SAFE matrices of non-prestressed structures found in Treyssède (2008) and Treyssède and Laguerre (2010).

Under prestress, the expression (21) is checked in the Appendix by showing the equality between the energy velocity and the group velocity for propagating modes in undamped materials.

6. Validation for a helical spring

The purpose of this section is to validate the SAFE model for prestressed helical springs.

The dispersion curves of prestressed helical waveguides obtained from the SAFE model will be compared to results obtained by the authors in Frikha et al. (2011), here used as a reference. In Frikha et al. (2011) the propagation modes in helical beams under axial loads are computed based on a Timoshenko model approximation. This model is limited to large helix radius of curvature ($1/\kappa$) compared to the cross-section radius a. Moreover the static prestressed state is calculated from a non-linear analytical solution derived in Wahl (1963), which is valid only for large helix angle Φ ($\Phi \geq 65°$) and large ratio R/a ($R/a \geq 5$). The reader may refer to Frikha et al. (2011) for a detailed study of load effects for various angles and radii.

In this section, the following data are chosen: the initial parameters of the helix (without initial stress) are $R_i/a = 10$ and $\Phi_i = 75°$. The prestress corresponds to a macroscopic axial deformation: $E^E = 40\%$ and $E^T = 0$. It is important to note that with these data both the effects of prestress and geometry deformation are important and thus need to be properly accounted for, as shown in Frikha et al. (2011).

The static analysis of a helical waveguide with these data has been presented in Section 6.1 of Part 1, where local displacements have been computed. The prestress matrix $[\sigma_0]$ is then determined from these local displacements. The geometry deformation is taken into account in the SAFE method by integration on the deformed cross-section S_0 (updating the node position, see Section 4.2). Fig. 1 illustrates the initial and the updated cross-sections FE mesh under $E^E = 40\%$ and $E^T = 0$, yielding an updated lay angle $\Phi = 68.8°$ and helix radius $R/a = 9.71$.

In a low frequency range ($\omega a/c_s \in [0; 0.005]$), Fig. 2 shows the dimensionless dispersion curves, $\omega a/c_s$ vs. ka, obtained from the SAFE model, where $c_s = \sqrt{E/2\rho(1+\nu)}$ is the shear velocity with Poisson ratio ν equal to 0.3. Grey and

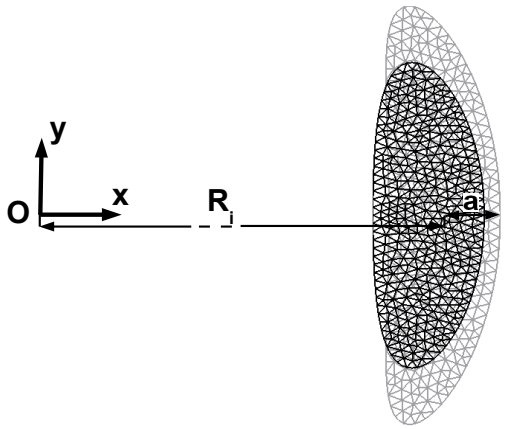

Figure 1: Cross-section FE mesh of a helical waveguide with $R_i/a = 10$ and $\Phi_i = 75°$. Grey: initial mesh ($E^E = 0$), black: updated mesh ($E^E = 40\%$), plotted in the initial and updated twisting coordinate system respectively.

black curves refer to unloaded ($E^E = 0$ and $E^T = 0$) and loaded ($E^E = 40\%$ and $E^T = 0$) cases, respectively. It can be observed that four modes are propagating in the frequency range considered. The tensile load has an effect on the four propagating modes. The load effect is found to be the most important for mode 2, its dispersion curve shifting to higher frequencies.

Figs. 3 and 4 compare the dispersion curves obtained from both SAFE method and the analytical model of Frikha et al. (2011) when the spring is loaded ($E^E = 40\%$ and $E^T = 0$). Good agreement is found between both models in the two frequency ranges $[0; 0.005]$ and $[0; 0.25]$. As shown in Frikha et al. (2011), the loading effect becomes smaller at higher frequencies. One points out that the wavenumber k presented in Figs. 2-4 is measured with respect to the curved helical axis, instead of the straight axis. This means that the wavenumber computed in the twisting basis with the SAFE method has been transformed to the helical system by multiplying ka with the ratio L/l where $l = \sqrt{L^2 + 4\pi^2 R^2}$ (see Treyssède and Laguerre (2010) for more details). This allows a direct comparison with the results of Frikha et al. (2011), obtained in a helical coordinate system.

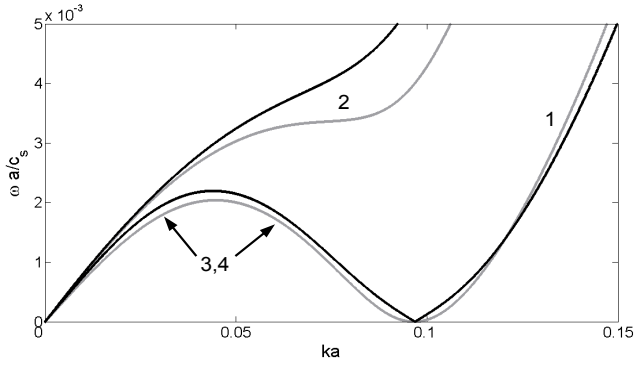

Figure 2: Plot of dimensionless frequency $\omega a/c_s$ vs. wavenumber ka for $R_i/a = 10$, $\Phi_i = 75°$, $\omega a/c_s \in [0; 0.005]$, $E^E = 0$ (grey) and $E^E = 40\%$ (black).

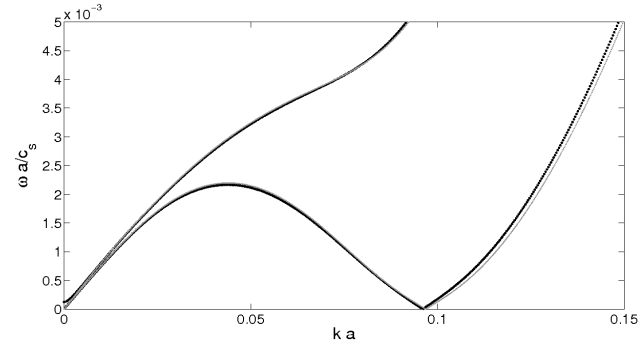

Figure 3: Plot of dimensionless frequency $\omega a/c_s$ vs. wavenumber ka for $R_i/a = 10$, $\Phi_i = 75°$, $\omega a/c_s \in [0; 0.005]$, $E^E = 40\%$. Grey: reference model, black: SAFE model.

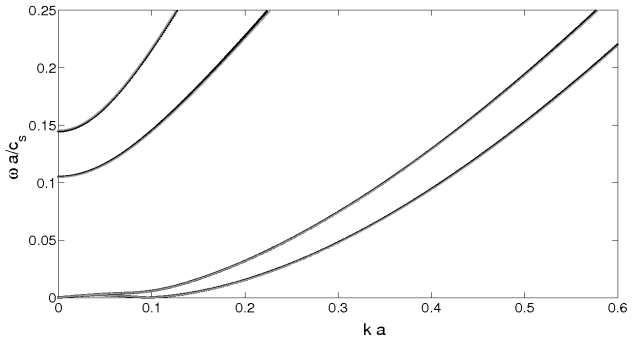

Figure 4: Plot of dimensionless frequency vs. wavenumber for $R_i/a = 10$, $\Phi_i = 75°$, $\omega a/c_s \in [0; 0.25]$, $E^E = 40\%$. Grey: reference model, black: SAFE model.

In Fig. 3, a slight difference for mode 1 and $ka \in [0.1; 0.15]$ is found between SAFE and analytical results. Note however that the static state is computed using a non-linear solution in the reference model while the SAFE model is linear. Moreover the analytical solution is based on a Timoshenko beam model while the SAFE method starts from a 3D formulation without beam assumption. Therefore, this difference is small for such a validation test, with a large load applied on a helical spring of large helix angle.

7. Dispersion analysis of seven-wire strands

In this section, results for guided wave propagation in multi-wire structures are presented. The study is restricted to seven-wire strands, with a central straight wire and one layer of six helical wires, for which some experimental data are available (Laguerre et al. (2002); Kwun et al. (1998)). In Laguerre et al. (2002), the effect of axial load on a seven-wire strand was studied for different axial loads of 2%, 10% and 60% of the Ultimate Tensile Strength (UTS). Experimental results showed the existence of a frequency band ('notch frequency') for different axial loads, where the first compressional mode does

not seem to propagate. For an unloaded strand with a nominal outer diameter $15.7mm$, the notch frequency is around $67kHz$. This frequency shifts to $88kHz$ under 60% of the UTS. Also in the experiments of Kwun et al. (1998), the notch frequency of a seven-wire strand was found to vary linearly with $\log(T)$, where T is the axial load.

Though numerical results will be presented in a dimensionless form, we focus on seven-wire strands with geometrical and material data experimented in the above-mentioned references. Thus in the following we will consider two strands which will be denoted Strand 1 and Strand 2. Characteristics are given in Table 1, the geometrical parameters corresponding to the initial configuration, without initial stress. For both strands, one will assume: $R_i/a = 1.967$, $\Phi_i = 7.9°$, $\nu = 0.28$ and $\rho = 7800\text{kg/m}^3$. As already explained in Part I, the contact between wires is modeled with perfect bonding conditions for simplicity (slip or friction effects are neglected).

Parameter	Strand 1	Strand 2
Nominal diameter (mm)	15.7	12.7
Core radius a (mm)	2.7	2.16
Young's modulus (Pa)	2.17e11	2.1e11

Table 1: Strand characteristics.

7.1. Preliminary results for unprestressed strands

In order to make this paper self-contained, the main results presented in Treyssède and Laguerre (2010), for strands without initial stress, and obtained with a SAFE method are recalled in this section.

Strand 1 is considered. There is no contact between two peripheral helical wires, and the contact between central and peripheral wires is assumed to be perfectly stick, see Part 1.

Dispersion curves have been computed by fixing a real wavenumber ka for the dimensionless frequency range $[0; 2]$. Fig. 5 presents the energy velocity vs. frequency curves for this unloaded seven-wire strand. Due to inter-wire coupling,

the dynamic behavior is quite complex compared to single-wire waveguides. Yet, a noticeable phenomenon can be observed: a veering frequency of the fastest mode occurs around $\omega a/c_s = 0.33$, corresponding to $65kHz$ for Strand 1. This veering frequency leads to an abrupt velocity decrease and the fastest mode corresponds to the first compressional-like mode in the strand, as shown in Treyssède and Laguerre (2010). Therefore, this veering frequency can be actually identified as the notch frequency observed in experiments, i.e. $67kHz$ (Laguerre et al. (2002); Treyssède and Laguerre (2010)).

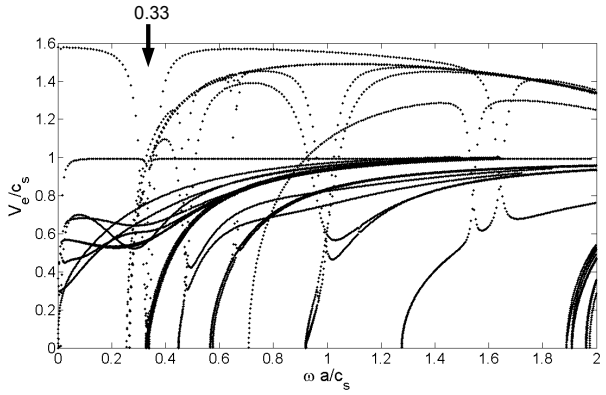

Figure 5: Dimensionless energy velocity V_e/c_s vs. frequency $\omega a/c_s$ for an unloaded seven-wire strand ($E^E = 0$).

Other experimental results are reported in Kwun et al. (1998) with a notch frequency found around $80kHz$. In that reference, the strand diameter is $12.7mm$. Using the SAFE approach with Strand 2, the dimensionless frequency $\omega a/c_s = 0.33$ yields a dimensional value of $79kHz$, which is again in good agreement with the experimental notch frequency.

In the following, the validation of the SAFE model proposed in this paper for loaded strands will be performed using the notch frequency as the quantity of interest, because experimental results are available.

7.2. Prestressed strand with line contact approximation

A seven-wire strand subjected to an axial tensile strain $E^E = 0.6\%$ ($E^T = 0$) is now considered. As a first step, one assumes that the contact area between the central and peripheral wires is a line, which is exact in the initial configuration (without any loading). This assumptions means a point-to-point contact for the 2D microscopic problem derived in the Part 1 of this paper. Moreover, this contact is supposed to be stick, see Part 1.

As in Section 6, the computation of modes of propagation in prestressed strands requires the computation of the static prestressed state, which is then used into the computation of propagation modes. Similarly to helical single wire waveguides, the static state has been already computed in Part 1, using the cross-section mesh of the unloaded strand (Fig. 6(a)). The nodes position is then updated to provide the mesh of the deformed cross-section S_0. Propagations modes are computed from this geometry.

The strand characteristics are those of Strand 1. Fig. 6(a) shows the superposition of the undeformed cross-section, in gray, and the updated mesh, in black. Differences between both meshes are negligible. In particular, Fig. 6(b) confirms that there is no contact between peripheral wires, even as a tensile load is applied.

Note that for better accuracy of numerical results, the mesh has been refined at contact points, yielding 17019 dofs. From the static solution given in Part 1, an axial strain of $E^E = 0.6\%$ (with $E^T = 0$) for this seven-wire strand corresponds to an axial force $T = 190.3kN$. This value provides a mean axial stress equal to $1260MPa$, corresponding to the mean stress applied in Laguerre et al. (2002) (i.e. 60% of the UTS).

Fig. 7 shows the dispersion curves (energy velocity vs. frequency). Except at low frequencies (below 0.1), we note that there is no difference between these results and those obtained for unloaded strand (see Fig. 5). In particular, the notch frequency remains around the dimensionless frequency $\omega a/c_s = 0.33$, as opposed to experimental results.

However a closer analysis of the deformed configuration due to the static

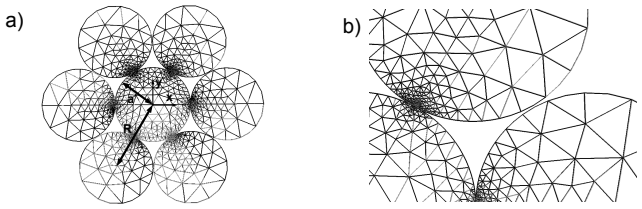

Figure 6: Cross-section FE mesh of a seven-wire strand with $R_i/a = 1.967$ and $\Phi_i = 7.9°$. Grey: initial mesh ($E^E = 0$), black: updated mesh ($E^E = 0.6\%$), plotted in the initial and updated twisting coordinate system respectively. (a): overview, (b): interwire view.

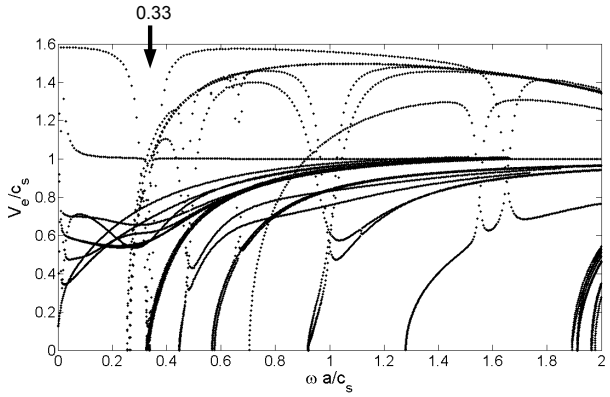

Figure 7: Dimensionless energy velocity V_e/c_s vs. frequency $\omega a/c_s$ for a seven-wire strand subjected to a tensile strain $E^E = 0.6\%$ with line contact approximation.

load in the wire-wire contact zone shows that the impenetrability condition is violated for the nodes in the vicinity of the contact points. This result is in line with Jiang et al. (2008) in which it is reported that contact area increases with the strand extension. Thus the line contact assumption is not valid and at this step it is suspected that this wrong assumption is responsible for the discrepancy between SAFE results and experimental data. Therefore hereafter a new model which properly takes into account the contact conditions will be used.

7.3. Surface Contact consideration

The new contact procedure is as follows. First, it has to be noticed that matching meshes are used for potentially contact lines of the central wire and each helical wire. This easily allows to address the line-to-line contact through individual node-to-node contacts for the 2D model. Thus contact pairs of nodes are formed on both sides of the initial point-to-point contact zone. Starting with the initial configuration from only one point-to-point contact between the core and each helical wire, the axial strain value gradually increases and the nodes position is updated. When the distance between the nodes of the same pair vanishes, the stick contact condition is imposed through the continuity of the displacement between these two nodes. Finally, when $E^E = 0.6\%$, we have obtained an updated geometry with eleven pairs of nodes in contact between the central wire and each peripheral wire.

With this contact procedure, note that a tensile strain $E^E = 0.6\%$ applied on a seven-wire strand with nominal diameter $15.7mm$ (Strand 1) yields a resultant force $T = 189.4kN$ and moment $M = 116.9N.m$. These values are quite close to those obtained in Part 1 from a point-to-point contact approximation: $T = 190.3kN$ and $M = 118.1N.m$. This is consistent with the results obtained in Ghoreishi et al. (2007), where it has been shown that the global static behavior is very little sensitive to contact assumptions.

Fig. 8 shows the energy velocity V_e/c_s with respect to the dimensionless frequency $\omega a/c_s$. Under an applied tensile strain $E^E = 0.6\%$, the notch frequency now shifts around the dimensionless frequency $\omega a/c_s = 0.44$. This value corresponds to $86kHz$ for a seven-wire strand with a nominal diameter $15.7mm$, which is in good agreement with experimental results (approximately $88kHz$ in Laguerre et al. (2002)). If we compare these dispersion curves with those obtained in Fig. 7, we can conclude that the shift of the notch frequency is mainly due to contact effects and more precisely to the increasing of the contact area.

As shown for unloaded strands in Treyssède and Laguerre (2010), the notch frequency phenomenon corresponds to a veering frequency between two extensional modes interchanging their behavior. Under axial loads, one can check

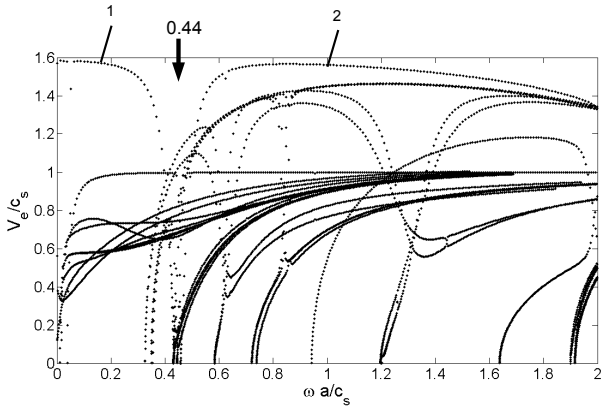

Figure 8: Dimensionless energy velocity V_e/c_s vs. frequency $\omega a/c_s$ of a seven-wire strand subjected to a tensile strain $E^E = 0.6\%$ with surface contact consideration (no interpenetration).

that this phenomenon still occurs, as illustrated in Fig. 9 showing the mode shapes at points 1 and 2 (see Fig. 8), corresponding to solutions (ka, $\omega a/c_s$, V_e/c_s) = (0.1, 0.16, 1.57) and (0.60, 0.96, 1.56) respectively. These mode shapes are quite close to those found in Treyssède and Laguerre (2010). Indeed, modes 1 and 2 belong to two distinct branches. Their global axial motion confirms that they are compressional-like modes, which have interchanged their shapes (for more details, the reader may refer to Treyssède and Laguerre (2010)). However, these modes are not exactly similar because the real parts of their axial displacement have opposite signs.

Comparing the dispersion curves of a prestressed strand (Fig. 8) with the unprestressed ones (Fig. 5), at low frequencies ($\omega a/c_s < 0.1$), large differences are found for some fundamental branches. For instance, the torsional mode (which quickly tends to $V_e/c_s = 1$ at higher frequencies), is found to be very sensitive to the tensile load. However, these results need to be confirmed by experiments, which is beyond the scope of this paper. We can observe also that dispersion curves shift to higher frequencies under the effect of tensile load, even at high frequencies. Due to contact effects, this contrasts with the results

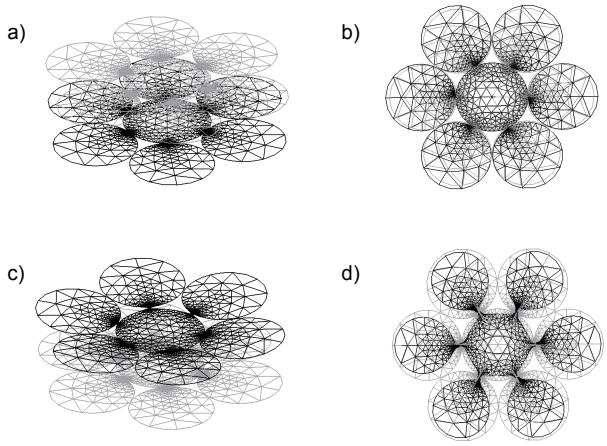

Figure 9: Mode shapes of a seven-wire strand subjected to a tensile strain $E^E = 0.6\%$ calculated at points 1, real (a) and imaginary (b) parts, and at point 2, real (c) and imaginary (d) parts. Grey meshes refer to the cross-section in its static configuration.

obtained for helical springs for which it was shown that the effects of axial load was significant only on low frequencies.

Finally, the SAFE results are now compared to other experimental results provided in Kwun et al. (1998), in which it has been found that the notch frequency varies linearly with $\log(T)$. Considering Strand 2, Fig. 10 shows the variation of the notch frequency as a function of the applied load computed from our SAFE model. The SAFE results have been obtained from the first node-to-node contacts formed on both side of initial contact points, yielding notch frequencies from 95 to 108 kHz in Fig. 10. Note that the low tension part of the experimental curve has not been explored with the numerical model because a much finer mesh would have been required around initial contact points. As it can be seen, the SAFE numerical results are in very good agreement with the experimental measurements of Kwun et al. (1998). The fact that the computed result for 100 kHz crosses the test result can be explained by simplifying assumptions used in the model (linear prestress state, frictionless contact).

Thus one can conclude to a validation of the SAFE approach with surface

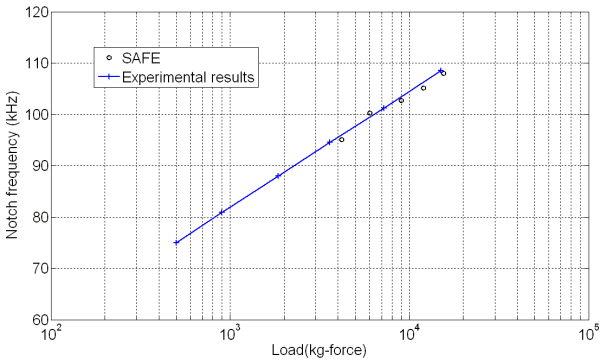

Figure 10: Variation of the notch frequency (kHz) vs. the applied load (kg-force) for a seven-wire strand of nominal diameter $12.7mm$. Circles: SAFE computation, crosses: experimental values of Kwun et al. (1998).

contact by comparison with the experimental results of Laguerre et al. (2002) and Kwun et al. (1998).

8. Conclusions

In this paper, elastic wave propagation in prestressed helical waveguides has been studied. The prestressed state is taken into account through the prestress (static Cauchy stress) and the deformed static geometry within an updated Lagrangian formulation. This prestressed static state, corresponding to axial loads, is computed thanks to the homogenization method proposed in Part 1 of this study. In Part 2, a SAFE formulation has been developed accounting for the translational invariance property, hence reducing the 3D elastodynamic equations of prestressed structures, written in the twisted coordinate system, to a 2D problem posed on the static deformed cross-section.

The present approach has been first applied to prestressed helical springs and the results have been compared to those obtained from an analytical solution based on a Timoshenko beam model. Good agreement has been found

on dispersion curves. Moreover it was shown that the effect of the prestressed state was significant at low frequencies.

Next a seven-wire strand subjected to axial loads has been considered. In this case the important role of the contact area has been highlighted, which thus requires its updating. Including this feature, we have shown that the SAFE model can reproduce experimental results with respect to the notch frequency of the fundamental compressional-like mode, which increases with the tensile load. From a physical point of view, a complex behavior is observed due to interwire coupling. Moreover, numerical results show that over a wide spectrum of frequencies, dispersion curves shift to high frequencies under the effect of tensile loads.

Appendix: Equality between group and energy velocities

For propagating modes in undamped materials, group and energy velocities of guided modes must be equal, as opposed to damped cases (Bernard et al. (2001)). Hence, let us assume that the material is undamped in order to show the equality between expressions (12) and (21).

Multiplying the eigenproblem (10) by $\{U\}^{T*}$, we get:

$$\begin{aligned}\{U\}^{T*}\left([K_{1\sigma}]+ik([K_{2\sigma}]-[K_{2\sigma}]^T)+k^2[K_{3\sigma}]\right)\{U\}\\ =\omega^2\{U\}^{T*}[M]\{U\}.\end{aligned} \tag{22}$$

This equation shows the equality between the kinetic and potential energies. Therefore, Eq. (18) becomes:

$$\int_{S_0}\overline{E}_k dS_0=\int_{S_0}\overline{E}_p dS_0=\frac{\omega^2}{4}Re(\{U\}^{T*}[M]\{U\}). \tag{23}$$

From Eqs. (20) and (23), the energy velocity expression (13) becomes:

$$V_e=\frac{Im\left(\{U\}^{T*}([K_{2\sigma}]^T+ik[K_{3\sigma}])\{U\}\right)}{\omega Re(\{U\}^{T*}[M]\{U\})}. \tag{24}$$

Besides, the imaginary part can be rewritten as:

$$
\begin{aligned}
&Im\left(\{U\}^{T*}([K_{2\sigma}]^T + ik[K_{3\sigma}])\{U\}\right) = \\
&\{U\}^{T*}\frac{1}{2i}([K_{2\sigma}]^T + ik[K_{3\sigma}])\{U\} - \\
&\{U\}^{T*}\frac{1}{2i}([K_{2\sigma}]^* - ik^*[K_{3\sigma}]^{T*})\{U\}.
\end{aligned}
\tag{25}
$$

For undamped materials, the matrix $[K_{3\sigma}]$ is real symmetric ($[K_{3\sigma}]^{T*} = [K_{3\sigma}]$ and the matrix $[K_{2\sigma}]$ is real ($[K_{2\sigma}]^* = [K_{2\sigma}]$). Then, Eq. (25) becomes:

$$
\begin{aligned}
&Im\{\{U\}^{T*}([K_{2\sigma}]^T + ik[K_{3\sigma}])\{U\}\} = \\
&\frac{1}{2}\{U\}^{T*}(i([K_{2\sigma}] - [K_{2\sigma}]^T) + (k + k^*)[K_{3\sigma}])\{U\}.
\end{aligned}
\tag{26}
$$

For propagating modes, wavenumbers are real ($k = k^*$) and Eq. (26) becomes equal to the numerator of the group velocity (12). Also, the denominator of Eq. (12) is always real because $[M]$ is real symmetric. Therefore, the energy velocity is equal to the group velocity.

References

Achenbach, J.D., 1973. Wave Propagation in Elastic Solids. North-Holland, Amsterdam.

Bartoli, I., Marzani, A., di Scalea, F.L., Viola, E., 2006. Modeling wave propagation in damped waveguides of arbitrary cross-section. Journal of Sound and Vibration 295, 685–707.

Bathe, K.J., 1996. Finite Element Procedures. Prentice Hall, Englewood Cliffs, New Jersey.

Benmeddour, F., Treyssède, F., Laguerre, L., 2011. Numerical modeling of guided wave interaction with non-axisymmetric cracks in elastic cylinders. International Journal of Solids and Structures 48, 764–774.

Bernard, A., Lowe, M.J.S., Deschamps, M., 2001. Guided waves energy velocity in absorbing and non-absorbing plates. Journal of the Acoustical Society of America 110, 186–196.

Chapelle, D., Bathe, K.J., 2003. The Finite Element Analysis of Shells-Fundamentals. Springer.

Chen, F., Wilcox, P.D., 2007. The effect of load on guided wave propagation. Ultrasonics 47, 111–122.

Damljanovic, V., Weaver, R.L., 2004. Propagating and evanescent elastic waves in cylindrical waveguides of arbitrary cross section. Journal of the Acoustical Society of America 115, 1572–1581.

Demma, A., Cawley, P., Lowe, M., Pavlakovic, B., 2005. The effect of bends on the propagation of guided waves in pipes. Journal of Pressure Vessel technology 127, 328–335.

Dong, S.B., Nelson, R.B., 1972. On natural vibrations and waves in laminated orthotropic plates. Journal of applied mechanics 39, 739–745.

Duhamel, D., Mace, B.R., Brennan, M.J., 2006. Finite element analysis of the vibrations of waveguides and periodic structures. Journal of sound and vibration 294, 205–220.

Finnveden, S., 2004. Evaluation of modal density and group velocity by a finite element method. Journal of Sound and Vibration 273, 51–75.

Finnveden, S., Fraggstedt, M., 2008. Waveguide finite elements for curved structures. Journal of Sound and Vibration 312, 644–671.

Frikha, A., Treyssède, F., Cartraud, P., 2011. Effect of axial load on the propagation of elastic waves in helical beams. Wave Motion 48, 83–92.

Gavric, L., 1995. Computation of propagative waves in free rail using a finite element technique. Journal of Sound and Vibration 185, 531–543.

Ghoreishi, S.R., Messager, T., Cartraud, P., Davies, P., 2007. Validity and limitations of linear analytical models for steel wire strands under axial loading, using a 3d fe model. International Journal of Mechanical Sciences 49, 1251–1261.

Gry, L., Gontier, C., 1997. Dynamic modelling of railway track: A periodic model based on a generalised beam formulation. Journal of sound and vibration 199, 531–558.

Hayashi, T., Tamayama, C., Murase, M., 2006. Wave structure analysis of guided waves in a bar with an arbitrary cross-section. Ultrasonics 41, 175–183.

Jezzine, K., 2006. Approche modale pour la simulation globale de contrôles nondestructifs par ondes élastiques guidées (Modal approach for the full simulation of nondestructive tests by elastic guided waves, in French). Ph.D. thesis. Université de Bordeaux.

Jiang, W.G., Warby, M.K., Henshall, J.L., 2008. Statically indeterminate contacts in axially loaded wire strand. European Journal of Mechanics A/Solids 27, 69–78.

Kwun, H., Bartels, K.A., Hanley, J.J., 1998. Effects of tensile loading on the properties of elastic-wave propagation in a strand. Journal of the Acoustical Society of America 103, 3370–3375.

Laguerre, L., Brissaud, M., Aime, J.C., 2002. Low-frequency ultrasound reflectometry device based on magnetoelastic transducers for the non destructive evaluation of steel rods and cables. Bulletin des Laboratoires des Ponts et Chaussées 239, 7–27.

Loveday, P.W., 2009. Semi-analytical finite element analysis of elastic waveguides subjected to axial loads. Ultrasonics 49, 298–300.

Marzani, A., 2008. Time-transient response for ultrasonic guided waves propagating in damped cylinders. International Journal of Solids and Structures 45, 6347–6368.

Mencik, J.M., Ichchou, M.N., 2007. Wave finite elements in guided elastodynamics with internal fluid. International Journal of Solids and Structures 44, 2148–2167.

Nicolet, A., Movchan, A.B., Geuzaine, C., Zolla, F., Guenneau, S., 2007. High order asymptotic analysis of twisted electrostatic problems. Physica B: Condensed Matter 394, 335–338.

Nicolet, A., Zola, F., 2007. Finite element analysis of helicoidal waveguides. Measurement and Technology 28, 67–70.

Nicolet, A., Zola, F., Guenneau, S., 2004. Modeling of twisted optical waveguides with edge elements. The European Physical Journal Applied Physics 28, 153–157.

Onipede, O., Dong, S.B., 1996. Propagating waves and end modes in pretwisted beams. Journal of Sound and Vibration 195, 313–330.

Rattanawangcharoen, N., Shah, A.H., Datta, S.K., 1992. Wave propagation in laminated composite circular cylinders. International Journal of Solids and Structures 29, 767–781.

Synge, J.L., Schild, A., 1978. Tensor Calculus. Dover.

Tisseur, F., Meerbergen, K., 2001. The quadratic eigenvalue problem. SIAM Review 43, 235–286.

Treyssède, F., 2007. Numerical investigation of elastic modes of propagation in helical waveguides. Journal of the Acoustical Society of America 121, 3398–3408.

Treyssède, F., 2008. Elastic waves in helical waveguides. Wave Motion 45, 457–470.

Treyssède, F., 2011. Mode propagation in curved waveguides and scattering by inhomogeneities: application to the elastodynamics of helical structures. Journal of the Acoustical Society of America 129, 1857–1868.

Treyssède, F., Laguerre, L., 2010. Investigation of elastic modes propagating in multi-wire helical waveguides. Journal of Sound and Vibration 329, 1702–1716.

Wahl, A.M., 1963. Mechanical Springs. Second Edition, Mc Graw-Hill, Inc., New York.

Wempner, G., 1981. Mechanics of Solids with Applications to Thin Bodies. Sijthoff and Noordhoff, The Netherlands.

Yang, Y.B., Kuo, S.R., 1994. Nonlinear Framed Structures. Simon and Schuster, Asia Pte Ltd.

Zhuang, W., Shah, A.H., Dong, S.B., 1999. Elastodynamic green's function for laminated anisotropic circular cylinders. Journal of applied mechanics 66, 665–674.